AXAF grating efficiency measurements with calibrated, non-imaging detectors

Daniel Dewey[a], Jeremy J. Drake[b], Richard J. Edgar[b], Kendra Michaud[b], and Pete Ratzlaff[b]

[a] Center for Space Research, M.I.T., Cambridge, MA 02139

[b] Harvard-Smithsonian Center for Astrophysics, Cambridge, MA 02138

ABSTRACT

In Phase 1 of AXAF testing at the X-Ray Calibration Facility (XRCF), calibrated flow proportional counters (FPCs) and solid-state detectors (SSDs) were used both in the focal plane and as beam-normalization detectors. This use of similar detectors in the beam and focal plane combined with detailed fitting of their pulse-height spectra allowed accurate measurements of the HRMA absolute effective area with minimum influence of source and detector effects.

This paper describes the application of these detectors and fitting techniques to the analysis of effective area and efficiency measurements of the AXAF transmission gratings, the High Energy Transmission Grating (HETG) and the Low Energy Transmission Grating (LETG). Because of the high dispersion of these gratings the analysis must be refined. Key additional ingredients are the inclusion of detailed X-ray source models of the K and L lines based on companion High-Speed Imager (HSI) microchannel-plate data and corrections to the data based on high-fidelity ray-trace simulations.

The XRCF-measured efficiency values that result from these analyses have systematic errors estimated in the 10–20 % range. Within these errors the measurements agree with the pre-XRCF laboratory-based efficiency models of the AXAF grating diffraction efficiencies.

Keywords: X-ray, diffraction, grating, calibration, detectors, spectroscopy

1. INTRODUCTION

The High Energy Transmission Grating (HETG) and Low Energy Transmission Grating (LETG) are science instruments that will operate with the High Resolution Mirror Assembly (HRMA) in NASA's Advanced X-ray Astrophysics Facility (AXAF). Either of these two grating assemblies can be inserted into the optical path just behind the HRMA and, through diffraction, deflect the converging rays by angles roughly proportional to their wavelength. By combining the HRMA's high angular resolution (of order 1 arc second) and the grating's large diffraction angles (as high as 100 arc seconds/Å), the HRMA-grating-detector systems are capable of spectral resolving powers up to $E/dE \approx 1000$ in the AXAF energy band.

Extensive ground calibration data involving the gratings were taken from December 1996 through April 1997 at NASA's MSFC X-Ray Calibration Facility (XRCF). An overview of this calibration[1] and preliminary grating performance results[2–5] have been presented. The XRCF calibration was broken into two main calibration phases. In Phase 1 the flight HRMA and flight gratings were present but the focal plane detectors were the non-flight HRMA X-ray Detection System (HXDS) detectors: Flow Proportional Counter[6] (FPC), Ge Solid State Detector[7] (SSD), or the High Speed Imager[8] (HSI). In Phase 2 the AXAF flight detectors were used as the readouts. In either case the beam was monitored with FPC and SSD Beam Normalization Detectors (BNDs).

Note that as XRCF analysis has progressed, papers of a narrower scope, such as this one and other HETG/XRCF papers in this volume,[9–13] are required to adequately present the detailed results. In this paper we report on progress towards the detailed analysis of the Phase 1 measurements which were designed to measure the grating effective area and efficiency using the FPC and SSD in the focal plane. First the general concepts of effective area and efficiency are reviewed; next the general XRCF Phase 1 measurement configuration is described including summary properties

Other author information: Send correspondence to D.D.: Email: dd@space.mit.edu; Telephone: 617-253-7244; Fax: 617-253-8084
Up-to-date information available at: **http://space.mit.edu/HETG/xrcf.html**

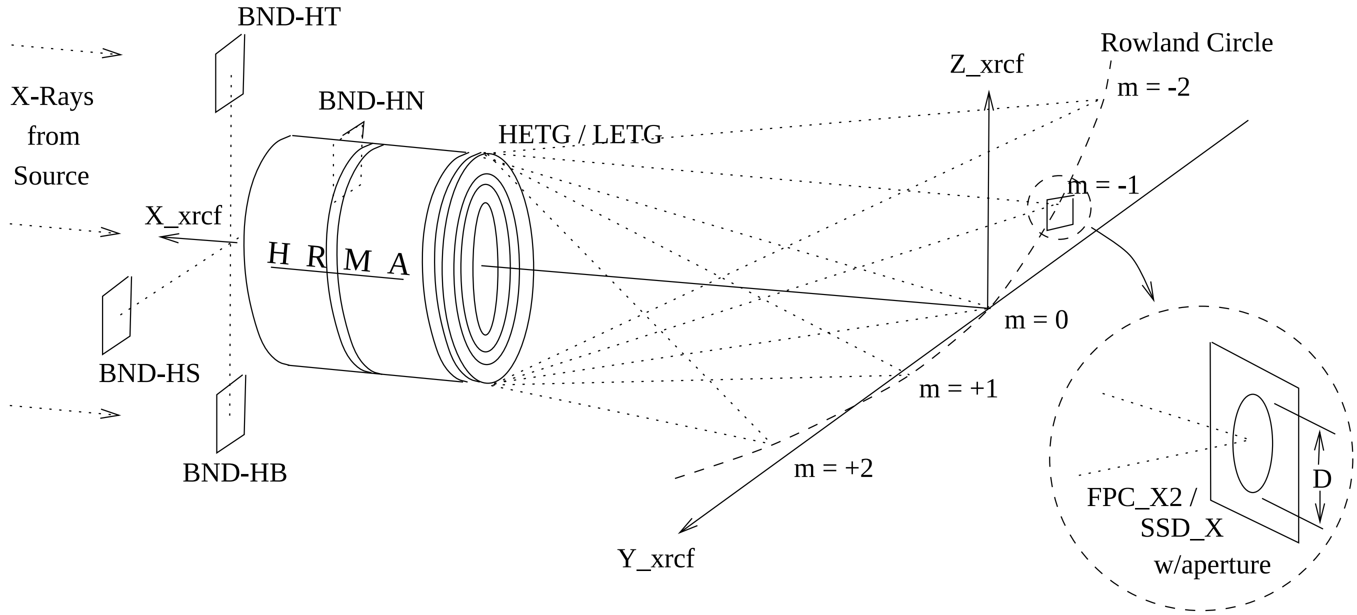

Figure 1. XRCF Schematic for Phase 1 Efficiency Measurements. The incident source flux is monitored by a set of beam monitor detectors (BNDs), four of which are located around the HRMA entrance aperture, shown at left. One or the other of the AXAF gratings, HETG or LETG, may be inserted into the converging HRMA beam. Detectors of similar design to the BNDs are located in the focal plane and can be positioned through 3-axes of motorized stages, *e.g.*, to follow the HEG Rowland circle shown by the dashed curve.

of the gratings and examples of the acquired data and their simplistic analysis. As will be demonstrated, analysis improvements require detailed knowledge of the source spectral composition which we derive from contemporary Phase 1 HRMA-grating-HSI observations of the source. Using the resulting spectra, accurate ray-traces of the system allow us to better understand the FPC/SSD data. Finally, analysis making use of the detailed source spectra and simulations is being carried out to derive accurate grating efficiency values and assess measurement errors.

2. BASIC DEFINITIONS

The mirror-grating response to an on-axis monochromatic point source consists of images in the various *diffracted orders* produced at locations given by the grating equation[14]:

$$sin(\beta) = \frac{m\lambda}{p} \tag{1}$$

where m is the order of diffraction (an integer $0, \pm1, \pm2, ...$), p is the grating period and β is the dispersion angle. This set of diffracted images is indicated schematically in Figure 1; the Rowland geometry and grating image properties are described in more detail by Stage *et al.*.[9]

These multiple focal images are, for the most part, spatially well separated and so it is possible and convenient to describe the system by an effective area into each diffraction order. Specifically, it is useful to consider the *optic effective area (OEA)* which represents the ability of the optics to collect photons at energy $E_{\rm line}$ into order m:

$$OEA_{2\pi}(E_{\rm line}, m) = \frac{\text{focal plane photons/s in line}-\text{order}}{\text{source flux in line}} \quad [\frac{\text{photons/s}}{\text{photons/cm}^2\text{s}} = \text{cm}^2] \tag{2}$$

where we get the usual cm^2 units, as for example in the HRMA-only effective area analysis.[15] The subscript "2π" (steradians) is used to indicate that this is the effective area over the full focal plane (half sphere) behind the HRMA and includes all structure in the diffracted order, *e.g.*, LEG support structure pattern. Low-level scattering by the HETG,[11] however, is not considered a contribution to these integer diffraction orders.

From a modeling point of view, the optic effective area for the mirror-grating combination is calculated from the following terms:

$$OEA_{2\pi}(E_{\rm line}, m) = \sum_{s=1,3,4,6} A_s(E_{\rm line})\ G_s(E_{\rm line}, m) \tag{3}$$

Here the sum is over the HRMA mirror shells s; A_s is the optic effective area for HRMA shell s alone. $G_s(E, m)$ is the average diffraction efficiency for the gratings on shell s and is calculated from the individual facet efficiencies $g_f(E, m)$:

$$G_s(E, m) = \ \nu_s\ \frac{1}{N_s} \sum_{f \in \{s\}} \ g_f(E, m) \tag{4}$$

where N_s is the number of facets on shell s and ν_s is a unitless shell-by-shell vignetting factor to account for non-active area, *e.g.*, the inter-grating gaps. Laboratory-measurement-based values of $g_f(E, m)$ and ν_s are available for all of the HETG and LETG grating facets; these values are the pre-XRCF efficiency predictions which will be tested by the XRCF measurements.

Finally, it is useful to define the grating "effective efficiency" for combinations of more than a single HRMA shell:

$$G_{\rm config}(E, m) = \frac{\sum_{s \in \{\rm config\}} A_s(E)\ G_s(E, m)}{\sum_{s \in \{\rm config\}} A_s(E)} \tag{5}$$

where "config" stands for the HEG (shells 4,6), MEG (shells 1,3), or LEG (shells 1,3,4,6). In practice, it is these effective efficiencies of the configurations that are measured at XRCF.

3. PHASE 1 GRATING MEASUREMENTS: "WHAT'S THE PROBLEM?"

3.1. XRCF Hardware Configuration

A simple schematic of the relevant equipment is shown in Figure 1; an overview of XRCF testing is available in Weisskopf *et al.*[1] and other papers in the same volume. Brief, relevant descriptions of the key components are provided here:

BNDs: The beam normalization detectors (BNDs) monitor the source flux without the effects of the HRMA or HETG. There are six BND detectors: two, a Flow Proportional Counter (FPC) and a Ge solid state detector (SSD), are located 37.43 and 38.20 meters from the source in "Building 500", and four FPCs located 524 meters from the source surround the HRMA entrance aperture as indicated in Figure 1. To ensure some BND data are available over a wide range of source flux, apertures can be selected on the FPC_5, SSD_5, and FPC_HN BNDs.

Table 1. Useful XRCF Grating parameters. The values given here are based on sub-assembly and XRCF testing results.

Description	value	error	units
LETG Rowland spacing	8788.10	0.5	mm
HETG Rowland spacing	8782.8	0.5	mm
LEG average period	9912.16	0.99	Å
MEG average period	4001.41	0.10	Å
HEG average period	2000.81	0.05	Å
LEG angle	0.006	0.05	degrees
MEG angle	4.74	0.05	degrees
HEG angle	−5.19	0.05	degrees
(HEG+MEG)/2 angle	-0.225	0.05	degrees
MEG-HEG angle	9.934	0.008	degrees

Focal Plane Detectors: The FPC_X2 and SSD_X are non-imaging detectors with moderate energy resolution and have a variety of apertures used to isolate and measure grating-dispersed spectral features in the focal plane, *e.g.*, the aperture of diameter D in Figure 1. These detectors have well studied characteristics,[6,7] are similar to the BNDs, and provide some of the fundamental data for characterizing the efficiency and effective area of the system without the novelty of the flight-detectors.

Gratings: Relevant parameters of the AXAF gratings are given in Table 1. The four rings of facets on the LETG are designed to intercept and diffract X-rays from the corresponding four HRMA mirror shells. To preserve high diffraction efficiency at low energy, the LETG grating bars are held with a support mesh of coarse and fine periods which results in a weak diffraction pattern around each prime diffracted order.[2]

Because most of the high energy area of the HRMA is due to the inner two shells (4 and 6), very fine period (≈2000 Å) High Energy Grating (HEG) facets tile the HETG inner two rings. The outer two rings have Medium Energy Grating facets (MEG, ≈4000 Å period) that are efficiency-optimized below 2 keV; a photograph of the HETG is shown in Schulz *et al.*.[13] These two grating sets have their dispersion axes offset by ≈ 10 degrees from each other so that their spectra are spatially separated in the focal plane. The HEG and MEG grating bars are supported on polyimide membranes which introduces additional absorption at energies below 1 keV but do not otherwise modify the diffracted images.

Coordinate system: The HXDS coordinate system is aligned with the XRCF coordinates shown in Figure 1. These coordinates define the sign of the grating order m: "positive" orders are those on the $+Y_{\rm xrcf}$ side of the zero-order. Knowledge of the grating dispersion axis orientation and the grating-to-detector distance (the Rowland spacing) allows a conversion of the diffraction angle β of Equation (1) to a three-dimensional location in the focal plane coordinates with respect to the zero-order location.

3.2. Measurements and Example Data

In this paper we focus on the Phase 1 measurements that used the conventional electron impact X-ray source (EIPS) and that had either the FPC or SSD as the focal plane detector. There are of order 160 grating measurements of this kind and over 50 no-grating measurements of direct relevance.

The measurement process involved positioning the detector aperture D at one or more locations in the focal plane and acquiring simultaneous pulse-height spectra from the focal plane detector and the BNDs. We illustrate our analysis methods with example data sets taken with the Fe-L and Ti-K source lines, Table 2. Note that non-grating measurements were made as well (Grating = NONE) to allow a direct measurement of efficiency by dividing the grating-in by the grating-out effective areas.

Examples of the pulse-height spectra obtained for some of these Ti-K and Fe-L measurements are presented and described in Figures 2 and 3.

Table 2. XRCF Phase 1 Grating Effective Area Measurements at Ti-K and Fe-L. These measurements are used to illustrate the analysis. A two-mean-free-path source filter was used with these measurements to reduce above-line continuum. For the Ti-K measurements a $D = 2.0$ mm aperture was used; for the Fe-L measurements $D = 1.0$ mm. The BND detector FPC_HN was fully open for all measurements here except for '9.004 where it was closed to a nominal 36 mm diameter.

TRW-ID	Source	Shells	Grating	Orders	date/runid/iteration
E-IXF-3D-9.001	Ti-K,TiKx2	1,3,4,6	NONE	–	970203/111140i0
E-HXF-3D-10.001	"	4,6	HEG	1,2,3,0,-1,-2,-3	970203/111126i0–'i6
E-HXF-3D-10.002	"	1,3	MEG	1,2,3,0,-1,-2,-3	970203/111123i0–'i6
E-LXF-3D-9.004	"	1,3,4,6	LEG	1,-1	970203/111144i0,'i1
D-IXF-3D-11.003	Fe-L,Fex2	1,3	NONE	–	970110/108163i0
D-IXF-3D-11.004	"	4,6	NONE	–	970110/108164i0
D-HXF-3D-11.020	"	4,6	HEG	1,0,-1	970110/108161i0–'i2
D-HXF-3D-11.019	"	1,3	MEG	1,0,-1	970110/108162i0–'i2
D-LXF-3D-11.018	"	1,3,4,6	LEG	1,0,-1	970110/108165i0–'i2

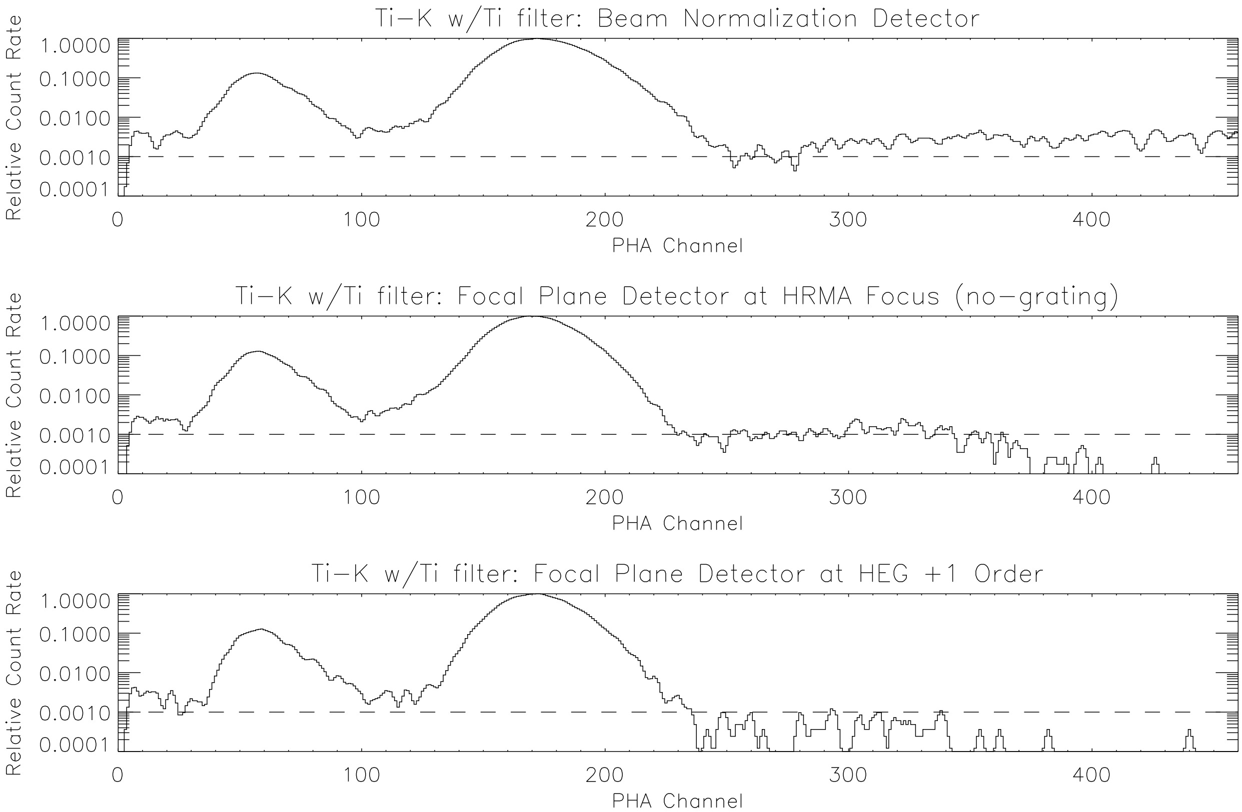

Figure 2. Examples of FPC Spectra for Ti-K Tests. The main features at this high energy, 4.51 keV, are the main photo-peak around channel 170 and the Ar escape peak around channel 60. *Top*: the spectrum seen by the BND FPC_HN directly viewing the source, continuum well-above the line energy is visible (channels 280 and up). *Middle*: the spectrum from FPC_X2 in the focal plane after the HRMA (no grating): the high-energy cutoff of the HRMA is visible in the continuum above channel 370. *Bottom*: the spectrum at the HEG $m = +1$ diffraction order – the detector here is seeing an essentially monochromatic input of the Ti-Kα line. To better show the differences in continuum, the histograms here have been smoothed and a dashed reference line at a relative rate of 10^{-3} has been included.

3.3. Problems with Effective Area Analysis

A simple calculation of the measured optic effective area, Equation (2), from the pulse-height spectra would be:

$$OEA_D(E_{\rm line}, m) \quad = \quad \frac{R_{\rm fp}}{QE_{\rm fp}(E_{\rm line})} \Big/ \frac{R_{\rm BND}}{A_{\rm BND@HRMA} \ \times \ QE_{\rm BND}(E_{\rm line})} \tag{6}$$

The subscript D indicates the measured optic effective area is into a finite focal plane aperture. The detector rates R are the counts per second in the pulse height "bumps" and the BND effective area $A_{\rm BND@HRMA}$ is the equivalent geometric area of the BND detector at the HRMA aperture and, together with the quantum efficiencies QE, provides the absolute calibration.

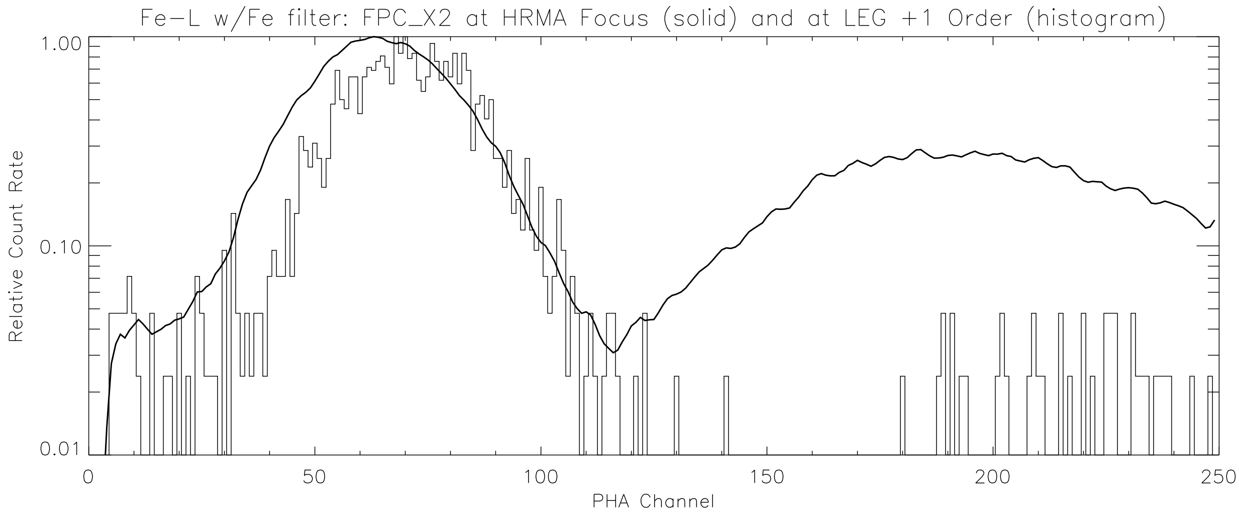

Figure 3. Examples of FPC Spectra for Fe-L Tests. The histogram-style curve shows the spectrum seen at the LEG $m = +1$ order: this is the monochromatic response to the 0.705 keV Fe-Lα line with some 2.1 keV $m = 3$ continuum counts around channel 220. The smoothed solid line shows the FPC_X2 spectrum at the HRMA focus without a grating (BND spectra are comparable): the "Fe-L bump" is visible peaking at channel 65 and continuum above the filter edge appears above channel 120. The extension of the bump to lower energies is due to the presence of unresolved lines, see Figure 5.

There is poor agreement between this simple analysis and our expectations especially for the dispersed $|m| = 1$ effective areas which are shown in Figure 4 and often appear lower than predicted. As the next sections will show, the source spectra often consist of multiple lines which are not resolved by the FPC detectors but are spatially separated in the focal plane by the grating diffraction. Thus, the BND is measuring several lines while the focal plane detector because of its finite aperture may be seeing only one or a fraction of the source lines. By measuring the source spectra and simulating the measurements we can implement improved analysis techniques.

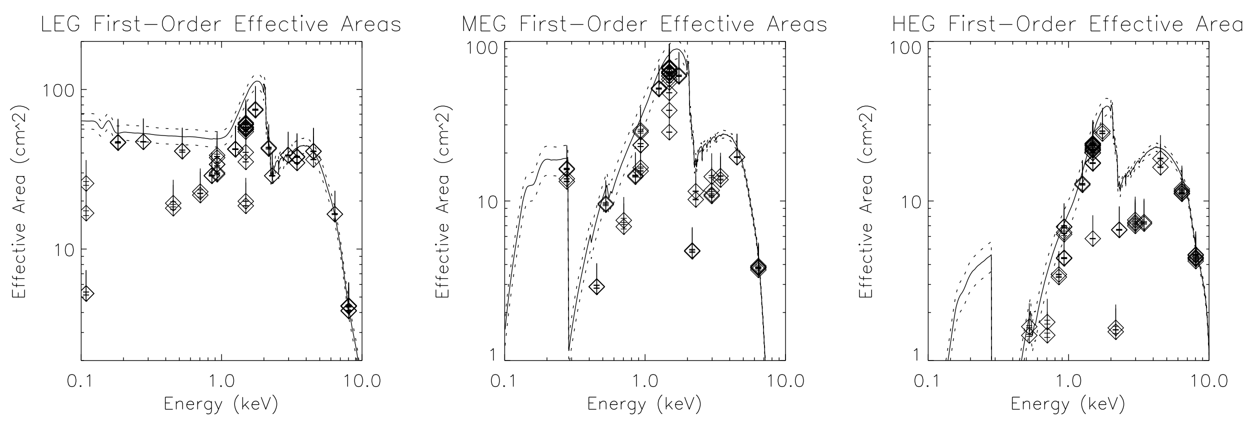

Figure 4. The problem with the standard effective area analysis: these plots show the grating first-order effective areas, calculated from simply extracted, uncorrected count rates, compared with model predictions[13]; these first-order effective areas are often measured low due to the presence of multiple and contaminating lines in the source spectrum.

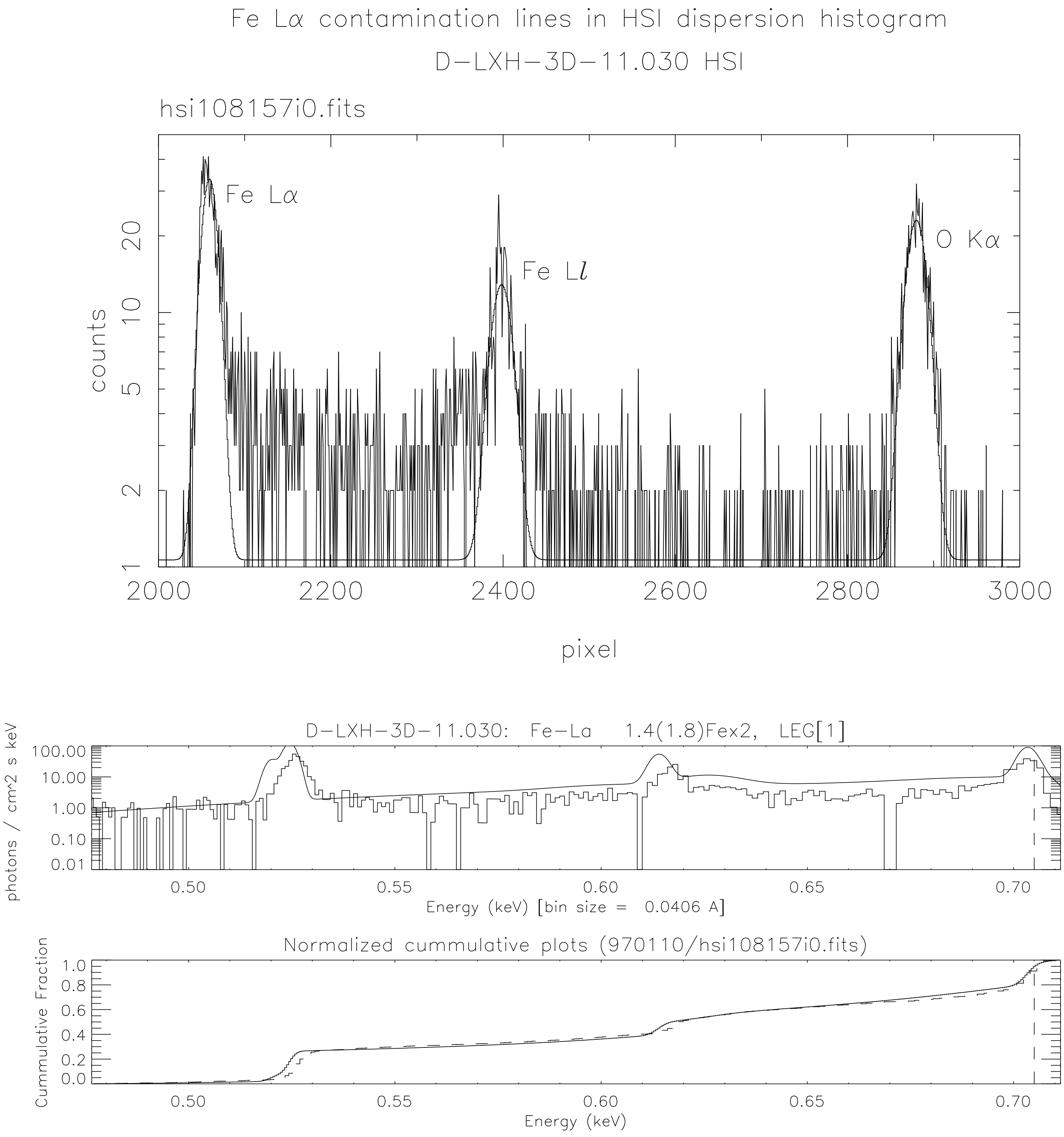

Figure 5. Fe-L line: LEG-HSI Spectrum and Model. *Top:* The High Speed Imager (HSI) positioned at the location of the LEG first-order for the Fe-Lα line; the detected events are binned by their location along the dispersion axis ($Y_{\rm xrcf}$). *Middle*: The counts spectrum is converted to a flux *vs.* energy spectrum using nominal calibration parameters for the HRMA, LEG, and HSI. A smooth model spectrum (see text) is plotted with the LEG-HSI spectrum. *Bottom*: The data (dashed) and model spectra (solid) are compared by plotting the cummulative (integrated) normalized flux within the observed energy range. This plot provides a comparison of the relative line (abrupt jumps) and continuum (sloping regions) fluxes in spite of data-model variations in line location, width, and overall normalization, *e.g.*, the small difference in measured *vs.* modeled energies due to inaccurate HSI position analysis.

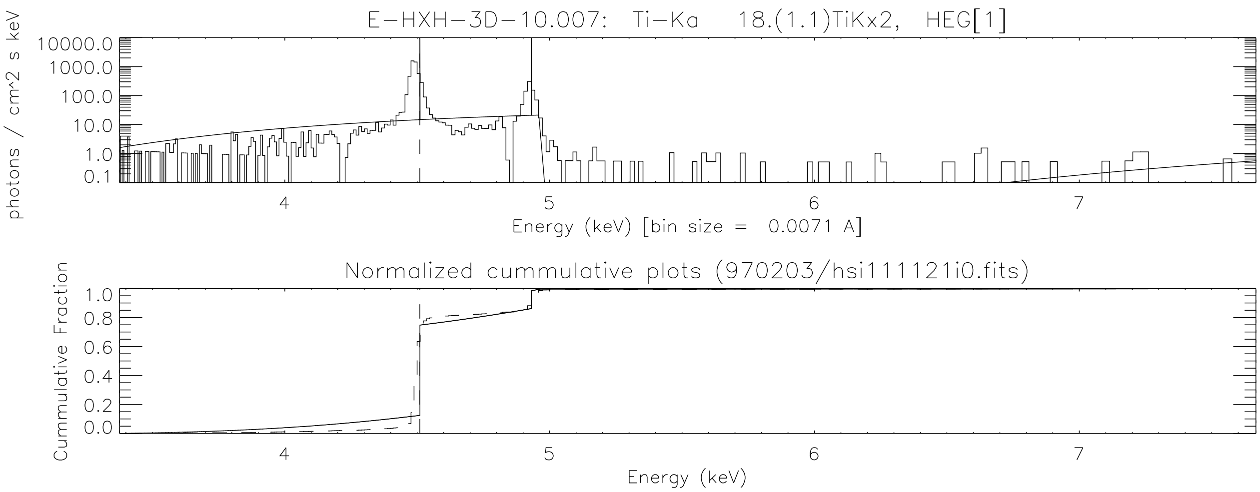

Figure 6. Ti-K line: HEG-HSI Spectrum and Model. *Top*: Measured Ti-K flux spectrum, calibrated by nominal parameters for the HRMA, HEG, and HSI; the Ti-Kα and Ti-Kβ lines are well resolved by the HEG dispersion. A model spectrum (solid) is plotted with the HEG-HSI-derived spectrum. *Bottom*: The data (dashed) and model (solid) spectra are compared by plotting the cummulative (integrated) normalized flux within the observed energy range. This plot provides a measured *vs.* modeled comparison of the relative line and continuum fluxes in spite of spectra differences, *e.g.*, here the measured and modeled line widths differ.

4. HIGH-RESOLUTION SOURCE SPECTRA

During Phase I calibration the HSI detector[8] provided imaging capability at high event rates. Companion HSI exposures were taken for most of the FPC/SSD effective area tests expressly for the purpose of being able to see the dispersed images that the focal plane aperture was sampling. Through application of the grating equation these images also yield high-resolution spectra of the sources; Fe-L and Ti-K HRMA-grating-HSI spectra are shown in Figures 5 and 6.

The model spectra plotted in these figures consist of a Kramer continuum[16] plus a number of Gaussian lines with widths and intensities set to approximate the HSI-measured spectra. The line energies are fixed at tabulated values for identified lines. Comparison of the measured and modeled spectra has been done by eye, facilitated by the use of normalized cummulative plots, examples of which are shown at the bottom of Figures 5 and 6. Generally we have spectra of these lines with all three AXAF gratings. Because of the high spectral resolution of the HRMA-grating systems, the actual line widths and shapes can be resolved for many lines especially with the MEG and HEG gratings, *e.g*, the Fe-L and O-K lines here. Other lines, like the Ti-K lines shown in Figure 6, are narrower than the instrument resolution and are modeled as delta functions.

5. RAY-TRACE SIMULATIONS

It would be straight forward to use the grating equation and parameters of the measurement to decide which region of the detailed source spectrum will fall in the detector aperture D. While this approach works, it has difficulty including a variety of effects such as: broad lines that may overfill the aperture D, HRMA and grating PSF effects which blur the events, higher grating diffraction orders of higher-energy source photons, and the LETG support structure diffraction pattern. In the end it is best to accurately model the complete source-HRMA-grating-detector system to completely understand what the detector sees.

The "Model of AXAF Response to X-rays" simulation package[17] (MARX, 2.04) has been used as the engine to produce these simulations. Custom IDL code was produced to create modified MARX parameters for a given XRCF measurement. Some items of note in this respect are:

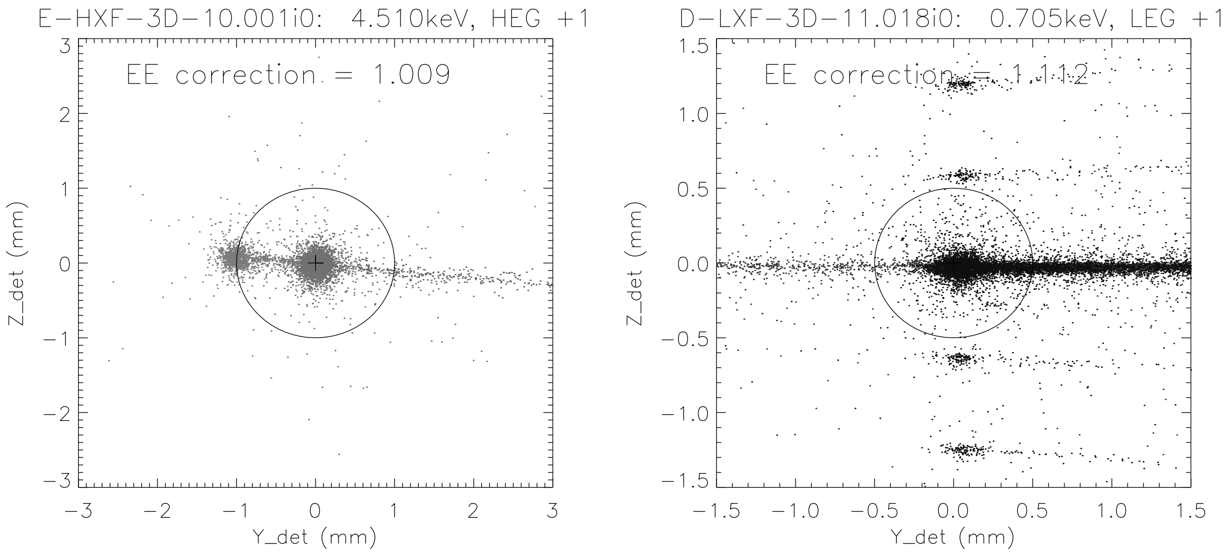

Figure 7. Ti-K and Fe-L simulated first-order images. In order to better undestand the FPC/SSD aperture measurements, the AXAF ray-trace package MARX was adapted to simulate XRCF measurements. These figures show the spatial distribution of events relative to the detector aperture used in the measurement. *Left*: The FPC aperture, 2 mm diameter circle, is centered on the Ti-Kα line; the Ti-Kβ line, at aperture edge, is partially included in the aperture and hence in the resulting pulse-height spectrum. The EE correction value of 1.009 indicates that very little of the Ti-Kα line flux is outside of the aperture. *Right*: Simulation of this Fe-Lα measurement clearly shows the LETG coarse-support diffraction pattern extending in the cross-dispersion direction, $Z_{\rm det}$. The bright continuum on the low-energy (right) side of the line is cut off by the Fe-L filter just above the line. The continuum streak to the high-energy side (left) of the Fe-Lα peak is actually 2.1 keV continuum that has been diffracted into the LEG +3 order.

- The modeled spectrum is used as the SpectrumFile with SourceFlux=0.0.
- Generally the ExposureTime is set to 0.0 and the simulation controlled by the NumRays.
- The source distance is set to 537.583 meters.
- A finite source size is modeled with SourceType="DISK" and S-DiskTheta1=0.0959.
- The nominal in-focus detector position is offset to -194.872 mm.
- The MARX grating RowlandDiameter is set to the actual XRCF value minus the 194.872 mm focus offset.
- To simulate the HXDS detectors, the HRC-I is used as the detector for its large, planar field. Additionally HRC-I-BlurSigma=0.0 and DetIdeal="yes".
- The IDL s/w post-processes the simulated events to apply the actual detector quantum efficiency.
- The MARX coordinates are flight coordinates and hence are rotated by 180 degrees about the X-axis from the XRCF coordinate system.

Simulated focal plane images for the the diffracted Ti-K and Fe-L lines are shown in Figure 7. These simulations can be used to calculate several quantities relevant to the efficiency measurements being analyzed here:

- The encircled energy correction value $EE_{\rm corr}$ is the ratio of the number of all line events to the number of line events that fall in the aperture.
- The pulse-height distribution of events that are within the detector aperture can be formed and used to estimate what fraction of the measured count rate is due to a given line or feature in the sectrum.
- The simulations can also be used to assess the sensitivity of either of the above values to variations in the aperture placement in the focal plane.

The use of these simulation-derived values is described in the context of our efficiency analysis in the next section.

6. IMPROVED DATA ANALYSIS

6.1. Analysis Formalism

Now that we've seen the source and aperture effects, it is clear that the "failure" of the analysis specified by Equation (6) is due primarilly to inaccurate or contaminated values for the measured rates and the effects of the aperture. In addition, the best estimate of the effective flux at the HRMA entrance requires a detailed beam uniformity analysis and consideration of data from all of the BND detectors. These effects are included in the revised equations:

$$OEA_{2\pi}(E_{\rm line}, m) = EE_{\rm corr} \times OEA_D(E_{\rm line}, m) = EE_{\rm corr} \times \frac{\mathcal{R}_{\rm fp}}{QE_{\rm fp}(E_{\rm line})} \Big/ F_{\rm effective}(E_{\rm line}) \tag{7}$$

$$F_{\rm effective}(E_{\rm line}) = \left\langle \frac{BU_{\rm corr}\ \mathcal{R}_{\rm BND}}{A_{\rm BND@HRMA} \times QE_{\rm BND}(E_{\rm line})} \right\rangle_{\rm BNDs} \tag{8}$$

where the $\mathcal{R}$'s are the rate in a specific line or narrow energy region, an explicit encircled energy correction factor, $EE_{\rm corr}$, converts from the count rate measured in an aperture to the total focal plane rate, and the incident flux is now an average over the properly weighted ($BU_{\rm corr}$) BND measurements taking into account beam uniformity variations.[18,19]

The grating effective diffraction efficiency, Equation (5), is measured as the ratio of the optic effective area with the grating in place to the optic effective area without the grating (HRMA-only):

$$G^{\rm meas}_{\rm config}(E_{\rm line}, m) = \frac{OEA^{\rm g}_{2\pi}(E_{\rm line}, m)}{OEA^{\rm H}_{2\pi}(E_{\rm line})} \tag{9}$$

where the g superscript refers to grating-in measurement and the H superscript is a HRMA-only measurement.

6.2. Count Rate Corrections

In general pulse-height analysis is performed to provide measured focal plane and BND rates, R, in some, possibly broad, energy range. A "line-fraction-correction" L, can be defined for each pulse-height spectrum to convert this measured rate to an estimate of the rate in a line or narrow energy region: $\mathcal{R} = L \times R$. The value of L can be numerically determined from the simulation of a measurement as the ratio $\mathcal{R}_{\rm sim}/R_{\rm sim}$; this requires precise definitions of $R_{\rm sim}$ and $\mathcal{R}_{\rm sim}$, however.

To determine $R_{\rm sim}$ from a simulation, the analysis method itself must be faithfully modeled. In order to determine $\mathcal{R}_{\rm sim}$, that is the count rate in the line, the "line" must be defined. Because some lines are in fact naturally broad and continuum is present in the modelled spectra, it is convenient instead to talk of a spectral "feature"; here a useful and reasonable definition of the feature is "all photons in the range $E_{\rm line} \pm E_{\rm line}/100$" – thus continuum under the line is part of the feature as well.

Substituting $\mathcal{R} = L \times R$ into Equation (9), many of the terms will (exactly or very nearly) cancel leaving:

$$G_{\rm config}(E_{\rm line}, m) = \frac{EE^g_{\rm corr}\ L^g_{\rm fp}}{EE^H_{\rm corr}\ L^H_{\rm fp}} \times \frac{R^g_{\rm fp}/(R^g_{\rm BND}/A^g_{\rm BND@HRMA})}{R^H_{\rm fp}/(R^H_{\rm BND}/A^H_{\rm BND@HRMA})} \tag{10}$$

Thus, the simple count-rate based efficiency, the ratio on the right, is corrected for after-the-fact by simulation-derived parameters. This "feature-fraction" correction (the product $EE_{\rm corr}\ L_{\rm fp}$) can be calculated and applied to different pulse-height analysis methods.

The next sections describe our specific analysis efforts that implement this approach to more accurately calculate the measured grating efficiency. In all cases the $EE_{\rm corr}$ factor is derived from the ray-traces and post-applied. Two of the analysis methods (ROI and "counts-in-bump") have non-trivial L values, the third method ("counts-in-line") includes the source spectral information "upstream" of the pulse-height analysis and so has $L = 1$.

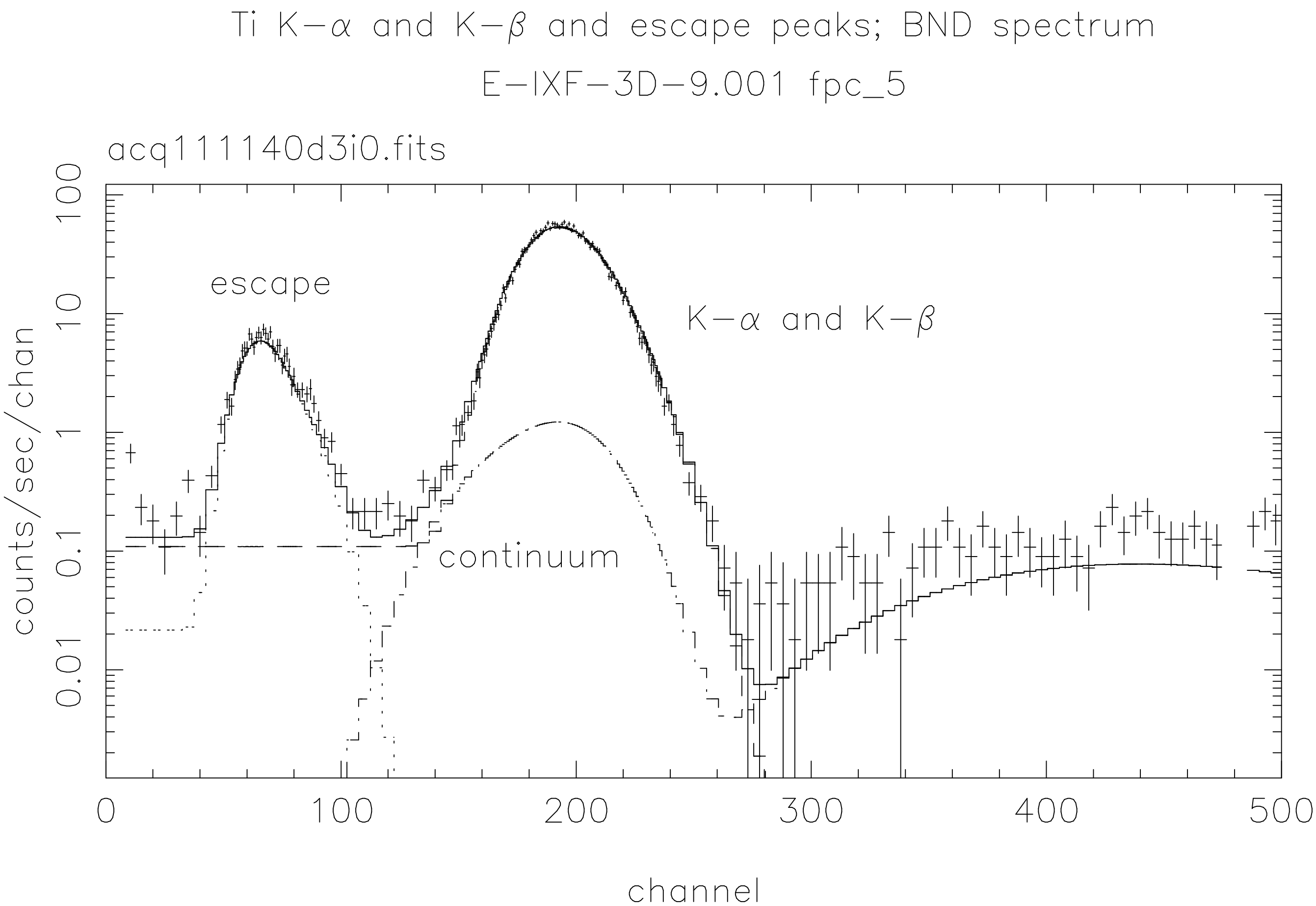

Figure 8. JMKMOD fit to Ti-K BND. Three of the components of the JMKMOD spectral model are highlighted here: the main Kα plus Kβ photo-peak, the Ar escape peak, and the broadband continuum generated by the source and given structure by the Ti source filter.

6.3. Region-of-interest (ROI) Analysis

The most simple pulse-height analysis method determines a count rate based on the total number of counts in a region of interest, for example the counts in channels 20 through 120 in the Fe-L spectra of Figure 3 may be summed. This has the advantage of simplicity and computational speed and robustness. Likewise the quantity R_{sim} can be generated with high accuracy for a coarse region of interest by counting all events in an energy range.

The very robustness of the ROI analysis points to its main defect: because the data are not evaluated with respect to any model there is no check that the assumed model is realistic (except perhaps when the ROI limits are viewed on the pulse-height histogram), errors in lines present, detector operation, continuum levels, etc. can all cause erroneous results without an indication of a "failure" of the assumptions.

For our purposes the ROI analysis with the corrections applied serves as an initial robust result and a sanity check and guide to the more complex and detailed fitting analyses, below. The results of the corrected ROI analysis are shown by the "x"s in Figure 10.

6.4. JMKMOD "counts-in-bump" Analysis

An improvement on the simple ROI analysis is the detailed pulse-height spectral fitting provided by the JMKMOD software.[20,21] This software is an add-on package to the XSPEC[22] x-ray spectral fitting package and was created to model the XRCF FPC and SSD detectors. Figure 8 shows the application of the JMKMOD model to a Ti-K BND spectrum. Because these detectors cannot resolve the Kα and Kβ peaks, the fitting process is not able to reliably

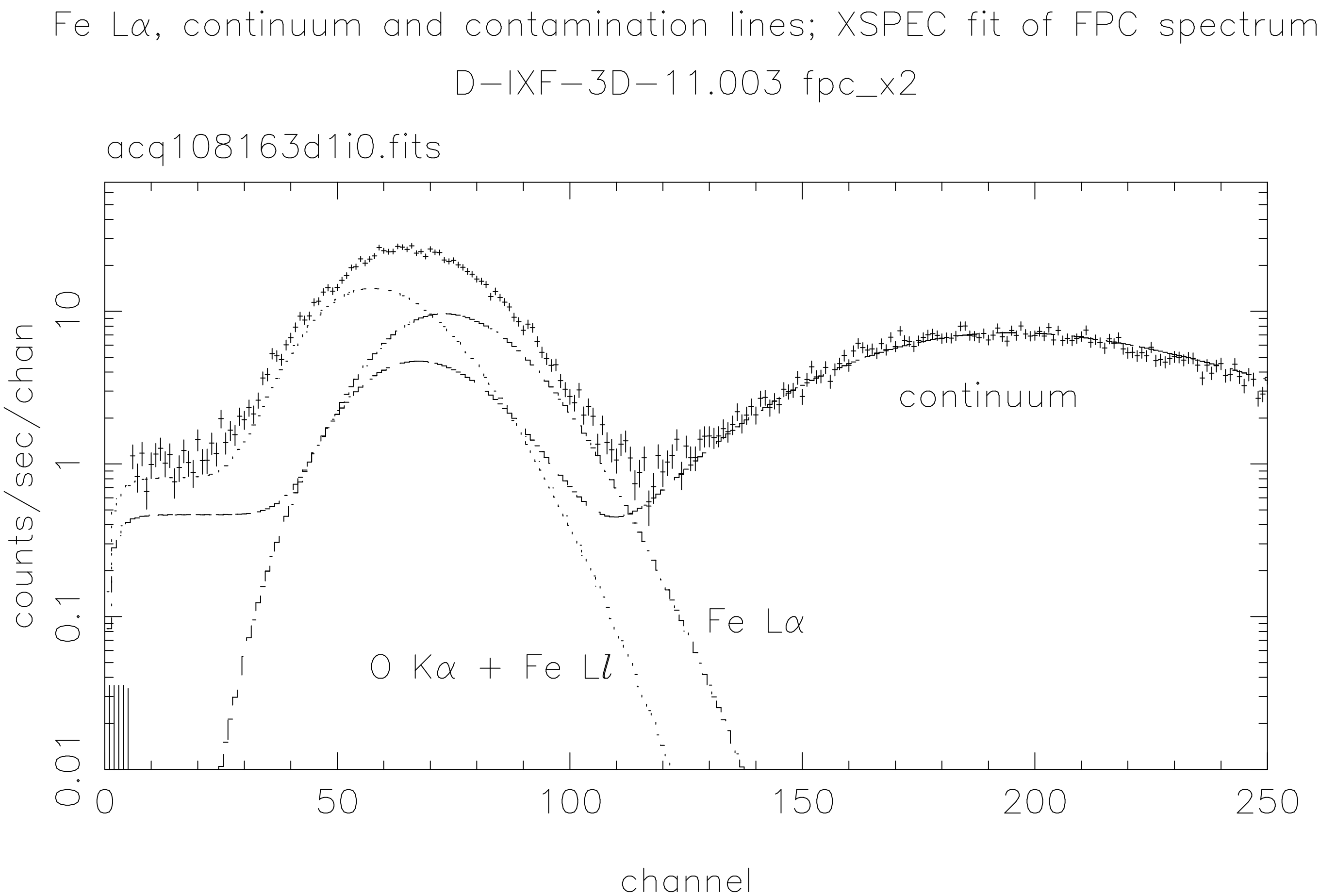

Figure 9. JMKMOD fit to Fe-L FPC_X2. In this "counts-in-line" analysis the three known source lines have had their relative intensities fixed based on the HSI-derived relative fluxes; the continuum component is allowed an independent normalization in the fit. The fit intensity of the Fe-Lα line is the rate in the line, that is $L = 1$ and $\mathcal{R} = R$. A good fit to the data indicates an agreement of the source model with the data to an accuracy allowed by the detector resolution and count statistics.

determine accurate count rates for the separate lines – rather the combined count rate in the Kα plus Kβ "bump" is determined.

Two main advantages of this fitting technique over a simple ROI analysis are: i) the measured data are fit by a model and therefore data quality and measurement assumptions are tested and ii) the continuum level in the spectrum is measured rather than depending on a modeled continuum.

The measured rate R is similar to the ROI rate but does not include a continuum contribution; this requires that slightly different values for the line fraction corrections L be applied in Equation (10). As a starting point, however, the efficiency results from this "counts-in-bump" analysis were corrected with the same correction as the ROI results and are shown in Figure 10 by the triangular symbols. As in the ROI case, the correction has the greatest effect on the efficiency of the L-lines of Mo, Ag, and Sn; its effect on the Ti-K HEG first-order efficiency is an increase of 9.3 %.

6.5. JMKMOD "counts-in-line" Analysis

Rather than applying the L line-fraction corrections to the rates in a region or bump, it is possible to fit the pulse-height spectra using as input a modeled source spectrum. Lines and features which are resolved in the spectrum can be fit with independent intensities; those that are poorly resolved must have their relative intensities fixed. This technique has the potential advantage over the "counts-in-bump" analysis in that the assumed model is directly tested against each pulse-height data set.

An example of a JMKMOD "counts-in-line" fit to a non-grating focal plane spectrum is shown in Figure 9. All three lines in the Fe-L spectrum, have had their relative intensities fixed based on the HSI counts spectrum, Figure 5, and modeled HSI, grating, HRMA, and FPC properties. The fit intensity of the Fe-Lα line is then directly the line rate, $\mathcal{R}$, *i.e.*, $L = 1$..

The only correction required to this analysis is the ratio $EE^{g}_{\rm corr}/EE^{H}_{\rm corr}$ which corrects for finite aperture effects; for LEG measurements this correction can be as much as a ≈ 10 % increase. For the dispersed orders of the broad low-energy lines (Be-K and B-K) this ratio must be calculated using an accurate source spectral line shape and source filter transmission curve.

The efficiency results of this "counts-in-line" analysis are shown by the square sysmbols in Figure 10.

7. CONCLUSIONS

The agreement of the XRCF-measured efficiencies with the laboratory-measurement-based efficiency predictions shown in Figure 10 is a wonderful confirmation of the grating diffraction models and facet-by-facet laboratory measurements: taken on their own, these XRCF Phase 1 EIPS measurements do in general verify the laboratory-based efficiency models at the 10–20 % level in most energy regions.

These analyses are nearly complete, what remains is to study and assign systematic errors to these measurements, *e.g.*, by obtaining error estimates for the HSI-derived source spectra and folding them through the analysis methods. Other potentially large systematic errors yet to be accounted for in the analyses are thought to originate in the FPC detectors in ways that are difficult to account for in the detector models. Apparently subtle effects, such as a bowing outward of the FPC windows due to internal gas pressure and obscuration and reflection of focussed focal plane light by the supporting wire mesh, are calculated to affect HRMA measurements at levels below a percent.[15] However, the former of these effects can be more important at the lowest energies where the detectors and windows are more optically thick: the window bowing alters the effective thickness and location of the window seen by incoming photons, and low energy photons penetrate to smaller depths in the detector. One of the next major challenges is to understand these detector effects and to account for them in the refined spectral modelling process (§6) in order to determine more accurate fluxes at the telescope aperture and focal plane.

In the case of the LETG, which is designed to operate at wavelengths as long as 170 Å (0.07 keV), the lowest energies available for efficiency and effective area measurements—provided by the B (183 eV) and Be (108 eV) EIPS—pose special difficulties because of the very low QE of the XRCF detectors in this regime. Here, detector background and counting statistics can be significant sources of error; during the Be tests for example, the HRMA BND count rates were generally too low to be of any quantitative use for beam monitoring and normalization, and the "Building 500" FPC detector provides the only means of determining the beam flux.

In the near future, these analysis techniques will be applied to the Phase 1 measurements made with a monochromator as the source in place of the EIPS source. The spectral analysis may in general be cleaner (no closely spaced L-lines for example), however the monochromators do have substantial beam uniformity variations[19] that must be dealt with.

The ultimate target of all our analyses is to produce grating efficiency models that are of sufficient accuracy that they are not a dominant source of uncertainty in the flight HRMA+grating+detector optical system. When all known sources of systematic error have been included in the modelling processes and flux determinations, it is hoped that the final uncertainties in the individual grating efficiency measurements will be as low as 2-3 %. At this level, the XRCF measurements will be capable of providing quite stringent tests of the grating efficiency models.

8. ACKNOWLEDGEMENTS

We extend thanks to the LETG team for providing their facet-by-facet laboratory data used in the LETG efficiency calculation here and to Norbert Schulz for providing helpful comments on the manuscript.

This work was supported in part by NASA under the HETG contract to the Massachusetts Institute of Technology, NAS-38249, and the Mission Support Team and the AXAF Science Center contracts to the Smithsonian Astrophysical Observatory, NAS8-40224 and NAS8-39073.

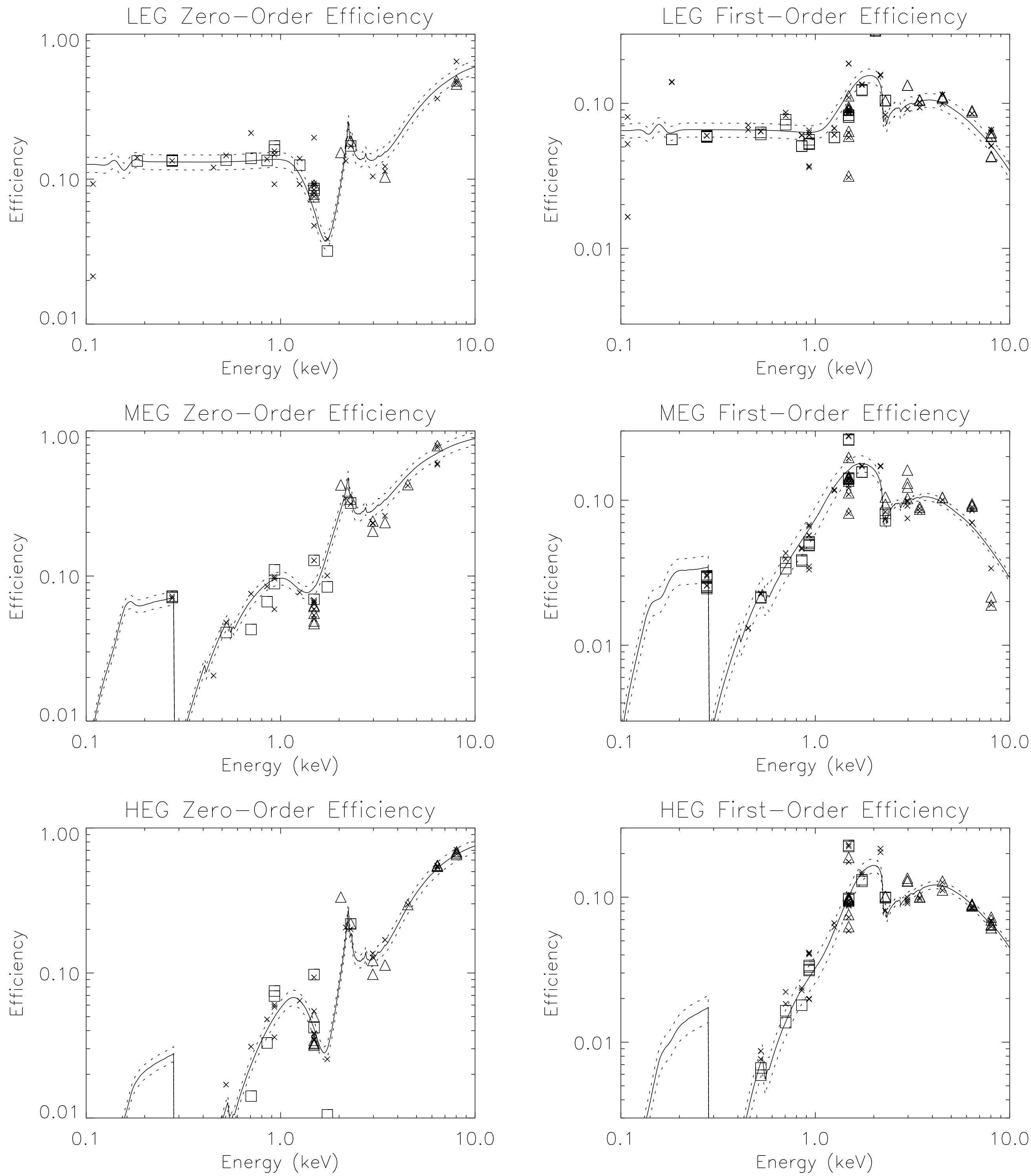

Figure 10. Efficiency Analysis Results. Measured efficiencies for the gratings in zero and first orders are shown here compared with the pre-XRCF model predictions, based on facet-by-facet laboratory measurements. The plotting symbols indicate the pulse-height analysis methods: "x"s are from region of interest rates (Section 6.3), triangles are from "counts-in-bump" rates (Section 6.4), and the squares are based on "counts-in-line" rates (Section 6.5). Statistical errors on the measurements are generally less than 3 %; understanding and reducing the systematic errors, here estimated to be of order 10–20 %, is an ongoing effort.

REFERENCES

1. M.C.Weisskopf and S.L. O'Dell, "Calibration of the AXAF observatory: overview", *Grazing Incidence and Multilayer X-Ray Optical Systems*, Proc. SPIE, Vol. **3113**, 2–17 (1997).
2. A.C. Brinkman, C.J.Th. Gunsing, J.S. Kaastra, H. Bräuninger, G. Hartner, P. Predehl, J.J. Drake, J.Z. Juda, M. Juda, D. Dewey, K.A. Flanagan, and H.L. Marshall, "Preliminary Test Results on Spectral Resolution of the Low Energy Transmission Grating Spectrometer on board of AXAF", *Grazing Incidence and Multilayer X-Ray Optical Systems*, Proc. SPIE, Vol. **3113**, 181–192 (1997).
3. D. Dewey, H.L. Marshall, K.A. Flanagan, C. Baluta, C.R. Canizares, D.S. Davis, J.E. Davis, T.T. Fang, D.P. Huenemoerder, J.H. Kastner, N.S. Schulz, M.W. Wise, J.J. Drake, J.Z. Juda, M. Juda, A.C. Brinkman, T. Gunsing, J. Kaastra, G. Hartner and P. Predehl, "Towards the Callibration of the HETG Effective Area", *Grazing Incidence and Multilayer X-Ray Optical Systems*, Proc. SPIE, Vol. **3113**, 144–159 (1997).
4. H.L. Marshall, D. Dewey, K.A. Flanagan, C. Baluta, C.R. Canizares, D.S. Davis, J.E. Davis, T.T. Fang, D.P. Huenemoerder, J.H. Kastner, H.L. Marshall, N.S. Schulz, M.W. Wise, J.J. Drake, J.Z. Juda, M. Juda, A.C. Brinkman, C.J.Th. Gunsing, and J.S. Kaastra, G. Hartner and P. Predehl, "Towards the Calibration of the HETG LRF", *Grazing Incidence and Multilayer X-Ray Optical Systems*, Proc. SPIE, Vol. **3113**, 160–171 (1997).
5. P. Predehl, H. Bräuninger, A.C. Brinkman, D. Dewey, J.J. Drake, K.A. Flanagan, C.J.Th. Gunsing, G. Hartner, J.Z. Juda, M. Juda, J. Kaastra, H.L. Marshall, and D. Swartz, "X-Ray Calibration of the AXAF Low Energy Transmission Grating Spectrometer: Effective Area", *Grazing Incidence and Multilayer X-Ray Optical Systems*, Proc. SPIE, Vol. **3113**, 172–180 (1997).
6. B.J. Wargelin, E.M. Kellogg, W.C. McDermott, I.N. Evans, and S.A. Vitek, "AXAF Calibration: The HXDS Flow Proportional Counters", *Grazing Incidence and Multilayer X-Ray Optical Systems*, Proc. SPIE, Vol. **3113**, 526–534 (1997).
7. W.C. McDermott, E.M. Kellogg, B.J. Wargelin, I.N. Evans, S.A. Vitek, E. Tsiang, D.A. Schwartz, R.J. Edgar, S. Kraft, F. Scholze, R. Thornagel, G. Ulm, M.C. Weisskopf, S.L. O'Dell, A.F. Tennant, J. Kolodziejczak, and G. Zirnstein, "AXAF HXDS germanium solid state detectors", *Grazing Incidence and Multilayer X-Ray Optical Systems*, Proc. SPIE, Vol. **3113**, 535–543 (1997).
8. I.N. Evans, E.M. Kellogg, W.C. McDermott, M.P. Ordway, J.M. Rosenberg, and B.J. Wargelin, "High Speed Imager AXAF Calibration Microchannel Plate Detector", *Grazing Incidence and Multilayer X-Ray Optical Systems*, Proc. SPIE, Vol. **3113**, 18–29 (1997).
9. M.D. Stage and D. Dewey, "Verifying the HETG Spectrometer Rowland Design", *X-Ray Optics, Instruments, and Missions*, Proc. SPIE, Vol. **3444**, (1998).
10. H.L. Marshall, D. Dewey, N.S. Schulz, and K.A. Flanagan, "Spectral Features in the AXAF HETGS Effective Area using High-signal Continuum Tests", *X-Ray Optics, Instruments, and Missions*, Proc. SPIE, Vol. **3444**, (1998).
11. J.E. Davis, H.L. Marshall, M.L. Schattenburg, D. Dewey, "Analysis and Modeling of Anomalous Scattering in the AXAF HETGS", *X-Ray Optics, Instruments, and Missions*, Proc. SPIE, Vol. **3444**, (1998).
12. K.A. Flanagan, N.S. Schulz, S.S. Murray, G.D. Hartner, and P. Predehl, "HETG High-order Diffraction Efficiency" *X-Ray Optics, Instruments, and Missions*, Proc. SPIE, Vol. **3444**, (1998).
13. N.S. Schulz, D. Dewey, H.L. Marshall, "Absolute Effective Areas of HETG", *X-Ray Optics, Instruments, and Missions*, Proc. SPIE, Vol. **3444**, (1998).
14. M. Born and E. Wolf, *Principles of Optics, Sixth Ed.*, pp. 401-414., Pergamon, New York, 1980.
15. E.M. Kellogg *et al.*, "Absolute calibration of the AXAF telescope effective area", *Grazing Incidence and Multilayer X-Ray Optical Systems*, Proc. SPIE, Vol. **3113**, 515–525 (1997).
16. D.Dewey, D.N. Humpheries, G.Y. McLean and D.A. Moschella, "Laboratory Calibration of X-ray Transmission Diffraction Gratings", *EUX, X-Ray, and Gamma-Ray Instrumentation for Astronomy V*, Proc. SPIE, Vol. **2280**, 257–271 (1994).
17. AXAF Science Center, `http://asc.harvard.edu`, "MARX 2.0 User Guide, Rev 1.0", ASC TD. 404, October 1997.
18. G.J. Patnaude, D. Pease, H. Donnelly, M. Juda, C. Jones, S.S. Murray, M.V. Zombeck, R.P. Kraft, A.T. Kenter, G.R. Meehan, D.A. Swartz, R.F. Elsner, "Effective Area of the AXAF High-Resolution Camera (HRC)", *X-Ray Optics, Instruments, and Missions*, Proc. SPIE, Vol. **3444**, (1998).

19. D.A. Swartz, R.F. Elsner, J.J. Kolodziejczak, S.L. O'Dell, A.F. Tennant, M.E. Sulkanen, M.C. Weisskopf, and R.J. Edgar, "Use of Monochromators for the Calibration of AXAF", *X-Ray Optics, Instruments, and Missions*, Proc. SPIE, Vol. **3444**, (1998).
20. R.J. Edgar, E.Y. Tsiang, A. Tennant, S. Vitek, and D. Swartz, "Spectral Fitting in AXAF Calibration Detectors", *Grazing Incidence and Multilayer X-Ray Optical Systems*, Proc. SPIE, Vol. **3113**, 124–131 (1997).
21. E.Y. Tsiang, R.E. Edgar, S. Vitek, and A. Tennant, "JMKMOD, a Software Suite within XSPEC for the Ground Calibration of AXAF", *Grazing Incidence and Multilayer X-Ray Optical Systems*, Proc. SPIE, Vol. **3113**, 132–141 (1997). `http://hea-www.harvard.edu/MST/simul/xrcf/XSPEC/jmkmod.html`
22. K.A. Arnaud, *et al.*, "XSPEC, An X-Ray Spectral Fitting Package", part of the XANADU software from NASA Goddard Space Flight Center, `http://legacy.gsfc.nasa.gov/`